Nanoscale

PAPER

View Article Online
View Journal | View Issue

Cite this: *Nanoscale*, 2022, **14**, 14169

Manipulating the crack path through the surface functional groups of MXenes†

Yu Chen,[a,d] Shengjie Tang[b] and Xin Yan *[a,c]

As newly developed 2D materials, due to their advanced physical/chemical properties and potential applications in energy storage, electromagnetic interference shielding, electronics and photon-detectors, MXenes have attracted extensive attention in recent years. MXenes are synthesized by selectively etching the A element from MAX phases using hydrochloric acid and lithium fluoride, so hardly any pure structures of MXenes (*e.g.* Ti_2C, T_3C_2) exist. Usually, the surfaces of MXenes are terminated by –OH, –F, –O or other surface terminations. However, fundamental knowledge of the mechanical properties of MXenes, especially the effect of different functional groups, is limited due to the difficulty in mechanical testing. In this work, we studied the mechanical properties of a series of MXenes with emphasis on the effect of the functional groups. We took the most common MXene $Ti_{n+1}C_nO_2$ and $Ti_{n+1}C_n(OH)_2$ as examples using molecular dynamics simulation. We evaluated the moduli of various MXenes and the influence of the functional groups. Besides, we studied the fracture behavior of MXenes with different functional groups. Based on our simulations, we found that the functional group did affect the mechanical and fracture properties. And we also proposed a possible approach to controlling the crack propagation path which would benefit the further design of nanodevices and nanocomposites.

Received 24th April 2022,
Accepted 31st August 2022

DOI: 10.1039/d2nr02235d

rsc.li/nanoscale

1. Introduction

MXenes are a novel type of transition metal-based 2D material. After they were first synthesised in 2011,[1] they have shown great potential in energy storage,[2–8] flexible electronics (including both sensors[9] and actuators[10]), electromagnetic interference shielding,[11–13] sterilization[14] and many other applications. Intense efforts are being dedicated to both understanding the basic science underlying the synthesis, the structures and the properties, and engineering advanced devices using MXenes. It is reported that the bare MXenes have been found to have a higher elastic constant than other 2D materials beyond graphene.[15] So aside from graphene, MXenes would be a great choice to be used as materials for nanodevices and as the reinforcement for nanocomposites.[15] To have an optimal design of nanodevices and nanocomposites, fundamental knowledge of MXene mechanical properties is required.

MXenes are obtained from MAX phases (layered parent ternary carbide and nitride crystals) and during the manufacturing process, layer A is removed using a strong etching solution. Due to the etching conditions in the preparation process, producing bare MXenes in experiments has been almost impossible until now, and the surface of the MXene is always terminated by a mixture of functional groups. The new formula will be written as $M_{n+1}X_nT_x$. In this chemical formula, T refers to the surface terminations, and can be oxygen, hydroxyl, fluorine and other groups.[16–18] Under the influence of surface terminations, the properties of MXenes vary a lot. For example, the magnetism of the functionalized Cr_2C and Cr_2N systems reduced and even disappeared (for Cr_2CO_2).[19] And the electronic properties of MXenes, such as the bandgaps,[19] can be tuned by changing the composition of the surface terminations.

The termination group may also contribute to the mechanical properties of MXenes. Lipatov *et al.*[20] measured the elastic modulus and the breaking strength of mono-layer and bi-layer $Ti_3C_2T_x$ terminated with –F, –O, and –OH groups using atomic force microscopy (AFM). As mentioned above, the difficulty of producing bare MXenes and MXenes terminated with a single type of group makes the investigation of the roles of different functional groups impossible in experiments. Molecular dynamics (MD) simulation is a powerful tool to study the

[a]*School of Mechanical Engineering and Automation, Beihang University, Beijing, China. E-mail: yan_xin@buaa.edu.cn*
[b]*Grote Industry, Madsonn, IN, USA*
[c]*School Advanced Manufacturing Center, Ningbo Institute of Technology, Beihang University, Ningbo, China*
[d]*The 52nd Research Institute of China Electronics Technology Group Corporation, Hangzhou, China*

† Electronic supplementary information (ESI) available. See DOI: https://doi.org/10.1039/d2nr02235d

mechanical properties and the structure evolution of low dimensional materials,[21] metals[22] and nanocomposites.[23] With MD simulation, the bare MXene $Ti_{n+1}C_n$,[15,24,25] and the oxygen terminated MXene (Ti_2CO_x)[26] were examined. Besides, the thermal dissipation of oxidized MXenes has been studied using MD simulation.[27] In addition, there are many reports of the mechanical properties of terminated MXenes obtained from DFT data[25,28–35] which included the influence of functional groups on the mechanical properties of MXenes. Although first-principles studies are accurate and powerful, the information they can provide is not sufficient due to the size limit. Thus, the knowledge regarding MXenes, especially the effect of functional groups and the fracture properties, is still limited which has obstructed the further understanding of the MXene failure mechanism and the designing of nanocomposites/devices.

In this work, we first investigated the effect of the terminal group on the mechanical properties of the most common MXenes ($T_{n+1}C_nT_x$) *via* classical molecular dynamics simulation. Then, we focused on the fracture process of $Ti_3C_2T_x$ with loading in different directions. We also proposed a potential strategy to manipulate the crack pathway through the functional groups. We hope that our findings could provide a basic understanding of the functional groups' influence on the mechanical and fracture properties of surface-terminated MXenes, and benefit the design and property evaluation of nanodevices and nanocomposites using MXenes.

2. Methodology

Our MD simulation was performed using Large-scale Atomic/Molecular Massively Parallel Simulator (LAMMPS).[36] The structure of the bare MXene was anisotropic,[33] and this applied to the terminated MXenes too. The models of MXenes $Ti_{n+1}C_nT_2$ (n = 1, 2, 3, T = –OH, –O) were built from different types of primitive cell optimized by first-principles calculations.[19] The $Ti_{n+1}C_n$ system consists of 3/5/7 sheets with a hexagon-like unit cell, where the C layer was sandwiched between the two transition metal layers (the atomic structures of $Ti_{n+1}C_nT_2$ can be found in Fig. S1†). The functional groups –O/–OH were present on the surfaces of metal layers. Similar to graphene, the MXenes also had armchair and zigzag symmetric directions (Fig. S1†). With the help of the Open Visualization Tool (OVITO),[37] we obtained 6 models of MXenes terminated with a single functional group (–OH or –O). The size of the various models was about 22 nm by 22 nm (Fig. S1†), the thickness varied from 5.6 nm to 12.6 nm which depended on the number of layers of $Ti_{n+1}C_n$. The number of atoms ranged from 31 680 to 69 696.

In order to have a comprehensive understanding of the mechanical properties of MXenes, we employed the reaction force field (ReaxFF)[17] potential to describe the atomic interactions in MXenes, which provided a good description in functionalized MXenes. Correspondingly, the time step adopted in our simulation was 0.2 femtoseconds.

3. Results analysis

First, we studied the most popular MXene $Ti_3C_2T_x$. During the simulation, we applied periodic boundary conditions in the in-plane directions as shown in Fig. S1b,† and the z direction was kept free. Initially, we used an NVE ensemble and Berendsen thermostat to relax the monolayer MXene to achieve an equilibrium system at 300 K for 160 picoseconds (ps). Then we switched to an NPT ensemble to release the in-plane stress for 100 ps. Finally, we converted to an NVE ensemble and reused the Berendsen thermostat to maintain the temperature at 300 K. After 80 ps of relaxation, the MXene was stretched at a constant strain rate of 10^9 s^{-1} along the x or y direction, while the virial stress in the tensile direction was calculated. We noted that conventional MD simulation could not account for procedures in which the transition time exceeded one microsecond, thus the extreme strain rate of 10^9 s^{-1} was adopted. A series of algorithms, including the potential energy surface sampling approaches, have been successfully employed to assess the mechanical behavior of nanomaterials under a slow strain rate.[35,38–40] These techniques could be adopted in further investigations. Apart from the tensile tests, the simulation samples were also sheared at the same strain rate and the shear stress was calculated.

The tension and shear results of MXenes with –O (red line) and –OH (blue line) functional groups are shown in Fig. 1. The stress–strain curves obtained when loading the sample along the zigzag direction are found in Fig. 1a. After the linear and the non-linear stages, the systems reached the ultimate strength of 43.6 GPa for $Ti_3C_2O_2$ and 36.8 GPa for $Ti_3C_2(OH)_2$. After that, the stress dropped sharply to zero. Corresponding to different tensile stages, we extracted the structure diagrams of the three different strain stages (indicated on the stress–strain curves by yellow stars). As shown in the snapshots in the red and blue boxes in Fig. 1a, the atoms in the structure were colored according to their atomic shear strain magnitude at the specific strain stage. The color bar is shown in Fig. 1c and all the snapshots in Fig. 1 share the same color bar. We found that at the initial stage of the elastic deformation, different atoms were subjected to different degrees of strain, and the functional group atoms had a larger strain (the quantitative statistical results of average atomic shear strain are shown in Fig. 1b). When it came to the nonlinear-elastic deformation stage, the atomic shear strain of Ti and C atoms gradually increased (the color of the atoms becomes green in the middle snapshots in the red and blue boxes in Fig. 1a) and an X-shaped crack was initiated. At the failure stage, the crack of $Ti_3C_2O_2$ and $Ti_3C_2(OH)_2$ propagated along the zigzag directions. Derived from the linear part of the curves, the Young's moduli for $Ti_3C_2O_2$ and $Ti_3C_2(OH)_2$ were 409.1 GPa and 299.5 GPa respectively. The difference in Young's modulus could be attributed to the effect of the functional groups. The snapshots labeled as I, II, i and ii are the zoomed-in views of the black square areas in the second and third snapshots in the red and blue boxes, which represent the typical atomic shear strain variation of the structure before and after failure. We could tell

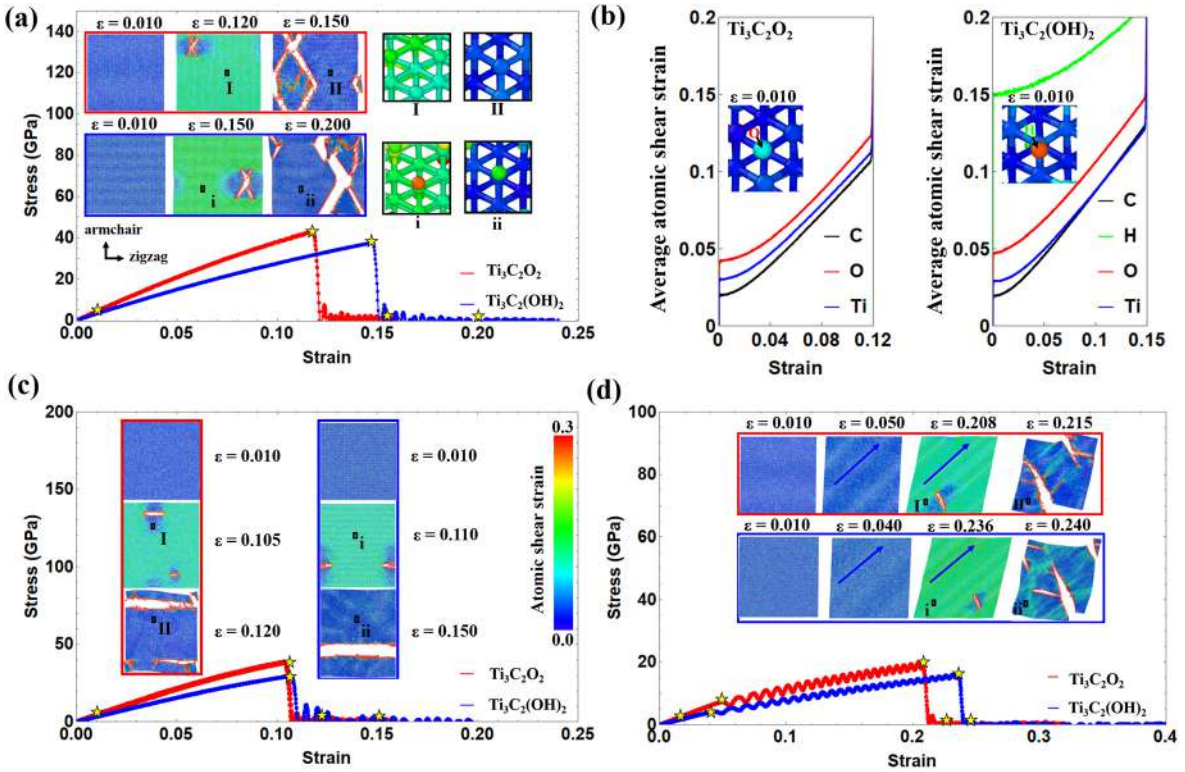

Fig. 1 The tensile and shear simulation results of $Ti_3C_2T_2$. (a) Stress–strain curves of stretching along the zigzag direction. The yellow stars indicate the strain stage of the snapshots. The snapshots are colored according to the atomic shear strain value with the color bar shown in the upper right corner of c. The snapshots in the red box correspond to the red curve of $Ti_3C_2O_2$ and the snapshots in the blue box correspond to the blue curve of $Ti_3C_2(OH)_2$. The snapshots on the right are the zoomed-in views of the black squares in the left snapshots. (b) Variation of the average shear strain of different atom types of $Ti_3C_2O_2$ and $Ti_3C_2(OH)_2$; (c) stress–strain curves with snapshots of stretching along the armchair direction; (d) stress–strain curves with snapshots of shear loading.

that for $Ti_3C_2O_2$ (red box and snapshots I and II), there were no significant differences between the atomic shear strain of the –O functional groups and the Ti/C atoms. While for $Ti_3C_2(OH)_2$ (blue box and snapshots i and ii), the atomic shear strain of the H atoms in the –OH functional groups was much higher compared to other types of atoms. A systematical analysis of the variation of the average atomic shear strain of different types of atoms is shown in Fig. 1b. During the tensile loading, the functional group atoms (O/H) had higher atomic shear strain compared with Ti/C atoms. The O atoms are light blue in the insets in Fig. 1b because of their higher atomic shear strain at the strain stage of $\varepsilon = 0.010$ for $Ti_3C_2O_2$. While for $Ti_3C_2(OH)_2$ at $\varepsilon = 0.010$, due to the extremely high atomic shear strain, the H atoms are even red. Based on the variation of average atomic shear strain of different types of atoms, the average shear strain of H atoms was 7.5 times that of C atoms. The difference in atomic shear strain among the different types of atoms was distinguished at the beginning of the loading, however, with the increase in the strain, the difference reduced. In particular, for Ti and C, the difference in the average atomic shear strain almost disappeared (Fig. 1b).

The stress–strain curves and corresponding snapshots during loading in the armchair direction are shown in Fig. 1c. Similar to Fig. 1a, the atoms in the snapshots are colored according to atomic shear strain. During loading, the samples went through linear and nonlinear stages as plotted in the stress–strain curves. Based on our simulation, $Ti_3C_2O_2$ had a higher Young's modulus (415.6 GPa) than $Ti_3C_2(OH)_2$ (315.2 GPa). This indicated that MXenes with both –O and –OH functional groups showed slightly anisotropic properties, and when loaded in the armchair directions, the MXenes behaved more stiffly (for the calculated results of the moduli of $Ti_{n+1}C_nT_2$, please refer to Fig. S2†). After that, in the nonlinear deformation stage, $Ti_3C_2O_2$ had a higher ultimate strength (39.8 GPa) than $Ti_3C_2(OH)_2$ (30.1 GPa). Different from loading in the zigzag direction, when the samples are loaded in the armchair direction, both $Ti_3C_2O_2$ and $Ti_3C_2(OH)_2$ reached their ultimate strength at a similar strain stage ($\varepsilon = 0.105$ for $Ti_3C_2O_2$ and $\varepsilon = 0.110$ for $Ti_3C_2(OH)_2$). Based on scrutiny of the snapshots, even though both $Ti_3C_2O_2$ and $Ti_3C_2(OH)_2$ samples initiated the crack along the same direction (zigzag), for $Ti_3C_2O_2$, the crack grew to form some small branches which were also along the zigzag direction. Besides, some disordered atom clusters formed together with the atomic chains or networks with the crack advancing and opening. Yet, this is not observed for $Ti_3C_2(OH)_2$ and a relatively clean crack was

formed. The zoomed-in views can be found in Fig. S3;† I, II, i and ii show the zoomed-in views of the structures before and after failure.

The results of shear loading are illustrated in Fig. 1d. Based on the stress–strain curves, the shear modulus of $Ti_3C_2O_2$ (155.6 GPa) was higher than that of $Ti_3C_2(OH)_2$ (103.2 GPa). During loading, the stress–strain curve rose until the MXene became wrinkled as shown in the insets (ε = 0.050 for $Ti_3C_2O_2$ in the red box and ε = 0.040 for $Ti_3C_2(OH)_2$ in the blue box, wrinkles are marked with blue arrows). The ultimate shear strength of $Ti_3C_2O_2$ was higher (19.7 GPa) compared with the strength of $Ti_3C_2(OH)_2$ (15.9 GPa). Thus, the existence of –OH groups actually weakened the strength of the MXene compared with the MXene with –O functional groups. When it came to the failure stage, the cracks of $Ti_3C_2T_x$ were initiated along the zigzag direction again which had a large angle with the wrinkle direction (blue arrows in the snapshots in Fig. 1d). After the crack propagated, there were multiple cracks along the zigzag directions. As shown in Fig. S4c,† the snapshots I, II, i and ii are the zoomed-in views of the black square areas in the third and fourth snapshots in the red and blue boxes (Fig. 1d), which represent the structures before and after failure. As shown in this group of snapshots, during loading, the atomic shear strain increased and after the failure, the atomic structure would maintain its sheared deformation. We noted that the fluctuation of the stress value was due to switching between two modes of buckling; further discussion can be found in ESI III.†

As mentioned before, the functional group atoms did contribute to the Young's modulus of MXenes, however the cracks of all MXenes were initiated and propagated along the zigzag direction in spite of different surface terminations. Due to this observation, it was reasonable to deduce that the crack propagation path depended on the Ti–C structure. To provide a more sophisticated understanding of the variation of Ti–C bonds during loading, we performed a systematical study of Ti–C bond and angle variation during the loading process. The zigzag and armchair directions were both evaluated to study the anisotropic properties. We took the $Ti_3C_2O_2$ structure which contained 3 layers of Ti atoms as an example and there were four types of Ti–C bonds. Bonds labeled as L_a and L_c connected the upper Ti atoms and C atoms, and bonds labeled by L_b and L_d connected the middle layer Ti atoms and the C atoms (Fig. 2a and b). From a structure symmetry point of view, L_a and L_c (L_b and L_d) were the same type of Ti–C bond, and had the same initial bond length. The difference between L_a and L_c is that with loading along the armchair (x) direction, L_a and L_d were parallel to the x-direction (armchair direction), but L_b and L_c were not. The view point of Fig. 2b is shown in Fig. 2a. In Fig. 2b, the α angle consists of L_a and L_b, and the β angle consists of L_a and L_c. We note that in Fig. 2b, the numbers mean the order of the distances when looking from the view point shown in Fig. 2a. The variations of the bond lengths and the angles during loading are plotted in Fig. 2c–f. If the samples were stretched in the zigzag direction (Fig. 2c and d), the length of L_b increased significantly (purple line in Fig. 2c). L_c had a similar angle with the loading direction when viewed from the x–y plane, however, it only fluctuated during loading without a significant changing of length. Thus, the length between the middle layer Ti and C was stretched the

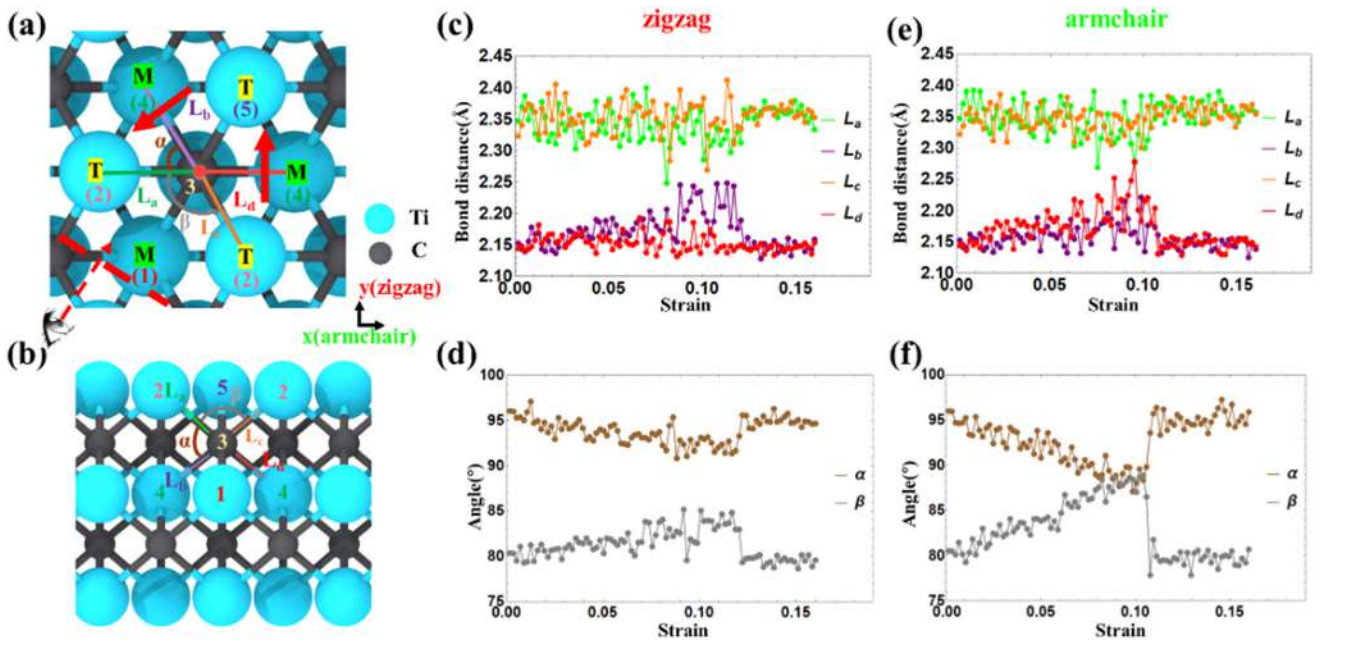

Fig. 2 Ti–C structure analysis of $Ti_3C_2O_2$ (a) and (b) a spatial display of bond lengths and bond angles. "T" and "M" represent the top layer and middle layer of Ti atoms respectively; figure (b) is viewed from the direction perpendicular to the red dashed line in (a), "1–5" represent the atom distance order from the view point. (c)–(f) The variation of bond length and bond angle when the samples were stretched in zigzag and armchair directions.

most before failure and correspondingly, angle α reduced and angle β increased (Fig. 2d). With loading along the armchair direction, L_d increased significantly (Fig. 2e), however L_a which was also along the armchair direction did not show a significant increase, but only fluctuated during loading. Correspondingly, angle α reduced and angle β increased (Fig. 2f). We noted that the middle layer Ti–C bonds L_b and L_d were the most stretched. These bonds were perpendicular to the zigzag directions. As a result, the crack would initiate and propagate along the zigzag direction (as shown by the red arrows in Fig. 2a) and this explains the crack propagation direction in Fig. 1. Although the bonds between the top layer Ti and C, L_a and L_c, had a similar orientation to L_b and L_d, the Ti atoms of the top layer were limited by the surface functional groups, and the length of the Ti–C bonds increased slightly in a fluctuating manner. All Ti–C bond lengths and Ti–C–Ti bond angles returned to and stabilized at the value of the initial undeformed bond length or angle after the samples were broken. Quantitatively, the increase in length of the most stretched bond (δL) in the armchair direction was 0.15 Å and δL in the zigzag direction was 0.10 Å. Meanwhile, the variation of the bond angle in the armchair direction (10°) was also larger than that in the zigzag direction (5°). Because of the structural symmetry of Ti_3C_2, L_a was equal to L_c, and L_b was equal to L_d. It could be inferred that the Ti_3C_2 structure sustained more severe structural deformation in armchair tension, so it would be more easily broken, which could be a validation of the higher ultimate strength when loaded in the zigzag direction of $Ti_3C_2T_x$ (please refer to Fig. 1a and c, as well as Fig. S2†).

From the previous observation, we found that when stretched in different directions, the tendency of the Ti–C bonds to break made the cracks of the MXene expand along the zigzag direction and the functional groups did affect the modulus of the MXene slightly. However, would the functional groups affect the fracture? To understand this question, we built another set of models with single functional group MXenes and a pre-crack was created on each model as shown in Fig. S5.† The dimensions of the model were approximately 22 nm × 11 nm in the x and y directions and the pre-crack size was 5 nm × 0.6 nm. A few layers of atoms were removed to create the pre-crack (Fig. S5a†). Only $Ti_3C_2T_x$ samples were considered in fracture testing. When the lower end was fixed, the top end was moved up and the sample was loaded at a strain rate of 10^9 s^{-1}. We adopted the J-integral to measure the breaking strength. The red area was for the calculation of the J-integral and the J-integral calculation followed the method reported in a recent publication.[41] The mode-I crack propagation simulation of $Ti_3C_2O_2$ and $Ti_3C_2(OH)_2$ along the zigzag and armchair directions is illustrated in Fig. 3a. When the sample was loaded along the zigzag direction (Fig. 3a, orange box), the initial crack was in the armchair direction. For $Ti_3C_2(OH)_2$, the crack path was relatively clean and it switched between the original armchair direction and the zigzag direc-

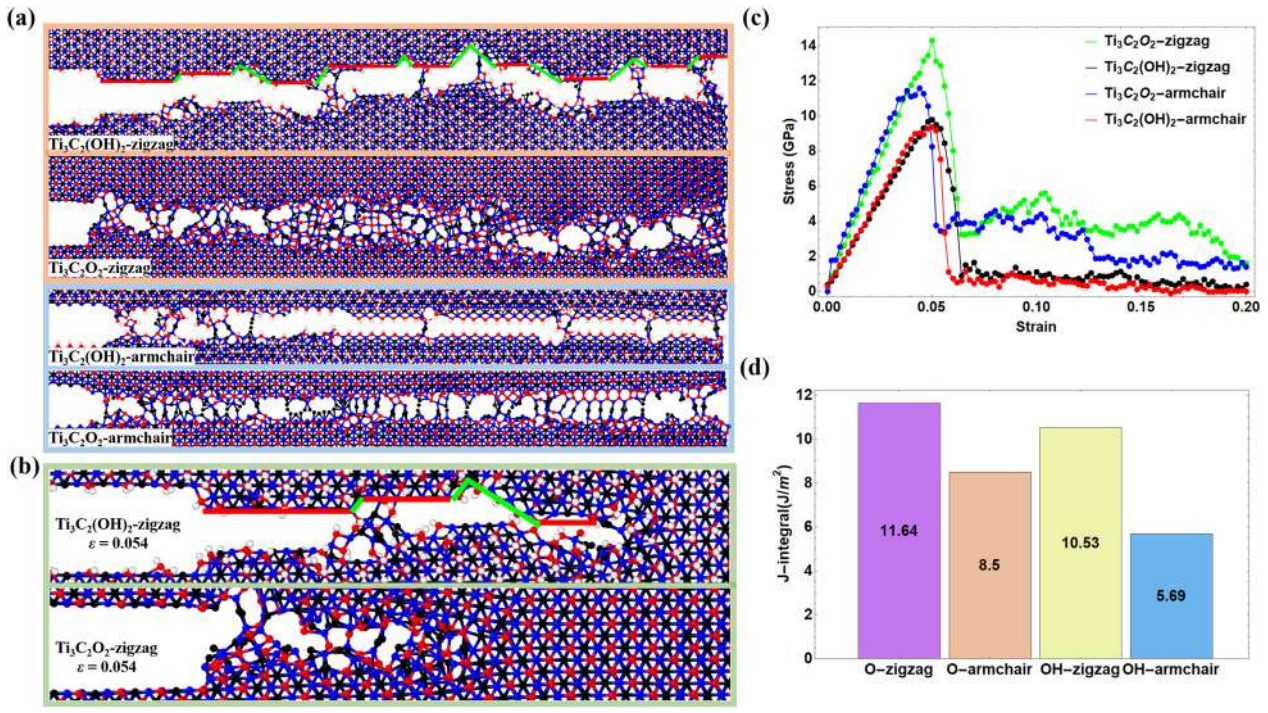

Fig. 3 The effect of functional groups and stretching direction on the fracture behavior. (a) Part of the snapshots of stretching along the armchair and zigzag directions for $Ti_3C_2O_2$ and $Ti_3C_2(OH)_2$; (b) zoomed-in views of stretching along the zigzag direction for $Ti_3C_2O_2$ and $Ti_3C_2(OH)_2$ at the initial stage of crack propagation (the strain stage of ε = 0.054); (c) stress–strain curves of fracture simulations for $Ti_3C_2O_2$ and $Ti_3C_2(OH)_2$ when loaded in the zigzag and armchair directions; (d) results of the J-integral when the cracks began to expand freely.

tion (as indicated by the red and green lines in Fig. 3a). For $Ti_3C_2O_2$, the crack path was very disordered; it moved sinuously with a lot of atom clusters and networks formed. When the loading direction was along the armchair direction (Fig. 3a, light blue box), the initial crack was in the zigzag direction, and the crack continued to expand directly along the zigzag direction for both $Ti_3C_2(OH)_2$ and $Ti_3C_2O_2$, even though for $Ti_3C_2O_2$, some atom networks were formed. In the crack propagation, we conducted a radial distribution function (RDF) analysis of the $Ti_3C_2(OH)_2$ and $Ti_3C_2O_2$ structures, particularly within the red box area as shown in Fig. S6a and b.† The RDF calculation results for $Ti_3C_2O_2$ before and after crack propagation are shown in Fig. S6c and d,† and the RDF calculation results for $Ti_3C_2(OH)_2$ are shown in Fig. S6e and f.† Comparing the plots in Fig. S6c and d,† we can tell that before the crack propagation, within the cutoff distance of 2.5 Å, only Ti–C and Ti–O bonds appear in the structure, however, after the crack propagation, within the same cutoff distance, newly formed C–C and C–O bonds appeared (black and red peaks). For the situation in $Ti_3C_2(OH)_2$ as shown in Fig. S6e and f,† there are no newly formed bonds before and after crack propagation and the type of peaks in the RDF before and after the crack propagation was the same. Besides, close scrutiny of Fig. S6c and d† revealed that the central position of the Ti–O peak moves 0.084 Å (the yellow dashed lines indicate the position of the peak) to the left after the crack propagated through the sample which indicates that some new Ti–O bonds have appeared. While for $Ti_3C_2(OH)_2$ the position of the peaks was basically at the same position before and after the crack propagation. Based on these observations, we could be able to draw the conclusion that for $Ti_3C_2O_2$, when the crack propagated through the sample, new C–C, C–O and Ti–O bonds appeared and formed chains and networks. While for $Ti_3C_2(OH)_2$, the bonds were thoroughly broken and the stress dropped directly to zero (Fig. 3c). In Fig. 3b, the zoomed-in views of the crack propagation (loading along the zigzag direction) at the strain stage of $\varepsilon = 0.054$ are illustrated. From these two snapshots, we can clearly capture the switch between armchair and zigzag directions for $Ti_3C_2(OH)_2$ and the formation of atom networks for $Ti_3C_2O_2$. By referring to the reported first-principles calculations,[19] which provided the required formation energy for Ti_3C_2 to be functionalized, the formation energy of $Ti_3C_2(OH)_2$ was −9.61 eV, while the formation energy of $Ti_3C_2O_2$ was −9.81 eV.[19] The greater the absolute value of the formation energy, the stronger the bond between the functional group atom and the Ti atom. This showed that it took more energy to break the bonds between the oxygen groups and the metal atoms. When $Ti_3C_2O_2$ was stretched, there was a strong binding energy between the –O functional groups and the Ti atoms, and more energy was required to destroy the connection of the Ti–O bond. So there will be more Ti–O bonds left between the fracture surfaces of $Ti_3C_2O_2$ as shown in Fig. 3b. From the corresponding stress–strain curve (Fig. 3c), we could find that after the fracture began to propagate (strain greater than 0.05 roughly), the stress for all cases sharply reduced. For $Ti_3C_2O_2$, there was a higher residual stress (4 GPa) left for both stretching directions, however, for $Ti_3C_2(OH)_2$, there was not much residual stress left. This corresponds to the observation in Fig. 3a and b. The J-integrals for the four cases are shown in Fig. 3d. Based on the comparison, we could tell that the breaking strength of $Ti_3C_2O_2$ was higher compared with $Ti_3C_2(OH)_2$. Besides, the breaking strength with loading along the zigzag direction was higher than that with loading along the armchair direction. This could be validated by our previous tensile testing results (Fig. 1) as well. The oxygen-containing MXene had a greater breaking strength and it was less likely to be broken when loaded in the zigzag direction compared to loading in the armchair direction.

Based on our previous calculation, we found that the functional group can somehow affect the mechanical properties and the fracture properties of MXenes. We wondered whether it was possible to manipulate the crack propagation path by varying the functional groups. To verify this suspicion, we created two models; both of them contained an interface between $Ti_3C_2(OH)_2$ and $Ti_3C_2O_2$. The angle between the interface and the initial crack was 60° (as shown in Fig. S7†). The difference between these two samples was the stretching direction. The left one was stretched along the armchair direction and the right one was stretched along the zigzag direction. When the sample was loaded along the armchair direction (Fig. 4a), the crack propagated straightly through the interface and the dominant broken bonds were L_d as shown in Fig. 4c. While when the sample was stretched along the zigzag direction, the initial crack was along the armchair direction (Fig. 4b). During loading, a sinuous crack path was formed and the crack had a deflection when going through the interface formed with different functional groups (yellow dashed line in Fig. 4b). Besides, some atom clusters formed after the crack propagated and evolved into several atomic chains or networks. These atomic chains and networks connected the fracture surfaces. In this way, the dominant broken bonds were L_b (Fig. 4d) and this caused the crack to propagate along the zigzag directions most of the time. The distribution of the absolute value of the stress in the y-direction (loading direction) at the point when the crack reached the interface is shown in Fig. 4e. We could tell that there was stress concentration at the interface, which caused the crack to expand along one of the zigzag directions (S1) in the $Ti_3C_2(OH)_2$ area. In addition, the σ_{yy} distribution on the middle cross-section (the black dashed line in Fig. 4e) is shown in Fig. 4f. In the $Ti_3C_2(OH)_2$ part, the Ti atoms of the middle layer and C atoms were under higher stress. While in the $Ti_3C_2O_2$ part, all atoms of every layer including the functional group atoms (O) were subjected to large stress. And we were also aware that the Young's modulus of $Ti_3C_2O_2$ was higher than that of $Ti_3C_2(OH)_2$, thus the $Ti_3C_2O_2$ part would have greater stress under the same strain. This uneven stress distribution in the atomic structure made the stress concentrate in the interface.

A further investigation was carried out based on models with $Ti_3C_2O_2$ and $Ti_3C_2(OH)_2$ placed in stacks (Fig. 5a). The initial crack was created in the middle of the sample along the armchair direction and in the area of $Ti_3C_2O_2$. With loading

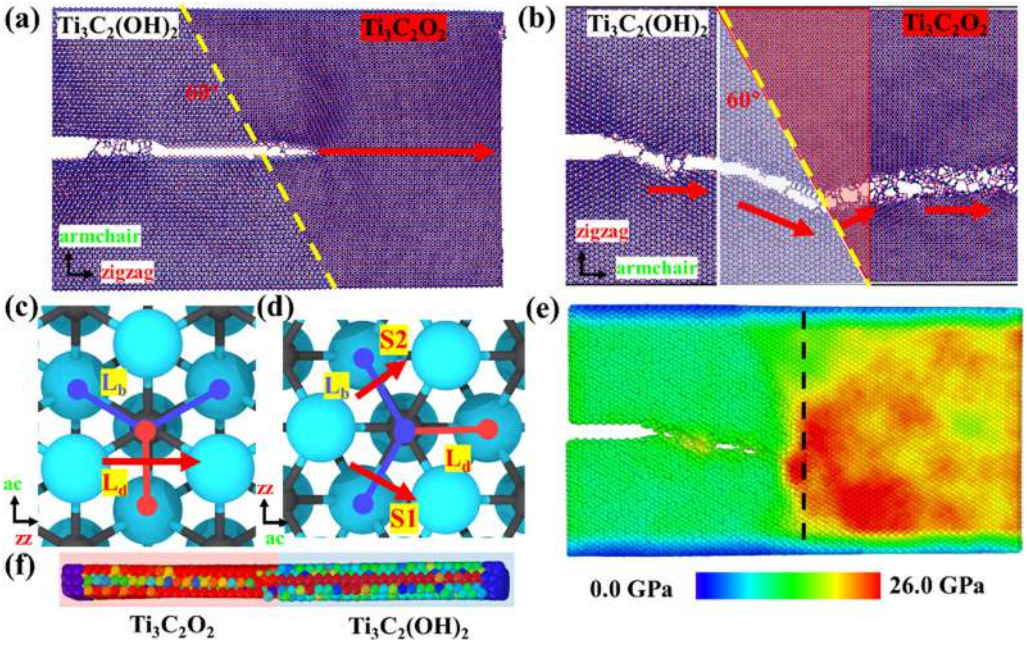

Fig. 4 The crack propagation through a functional group interface. (a) and (b) Loading along the armchair and zigzag directions. The yellow dashed line represents the interface. The left side of the interface is $Ti_3C_2(OH)_2$ and the right side is $Ti_3C_2O_2$. The red arrow indicates the direction of crack propagation, and the number represents the angle between the interface and the initial crack. (c) and (d) Zoomed-in views of the atomic structure and bonds when stretching along the armchair (ac) and zigzag (zz) directions, respectively. S1 and S2 represent two types of crack propagation directions. (e) The distribution of the average stress in the *y*-direction (σ_{yy}) when the crack reaches the interface. (f) Side view of σ_{yy} distribution, the red and blue dashed areas represent $Ti_3C_2O_2$ and $Ti_3C_2(OH)_2$, respectively. It shares the same color bar as shown in e.

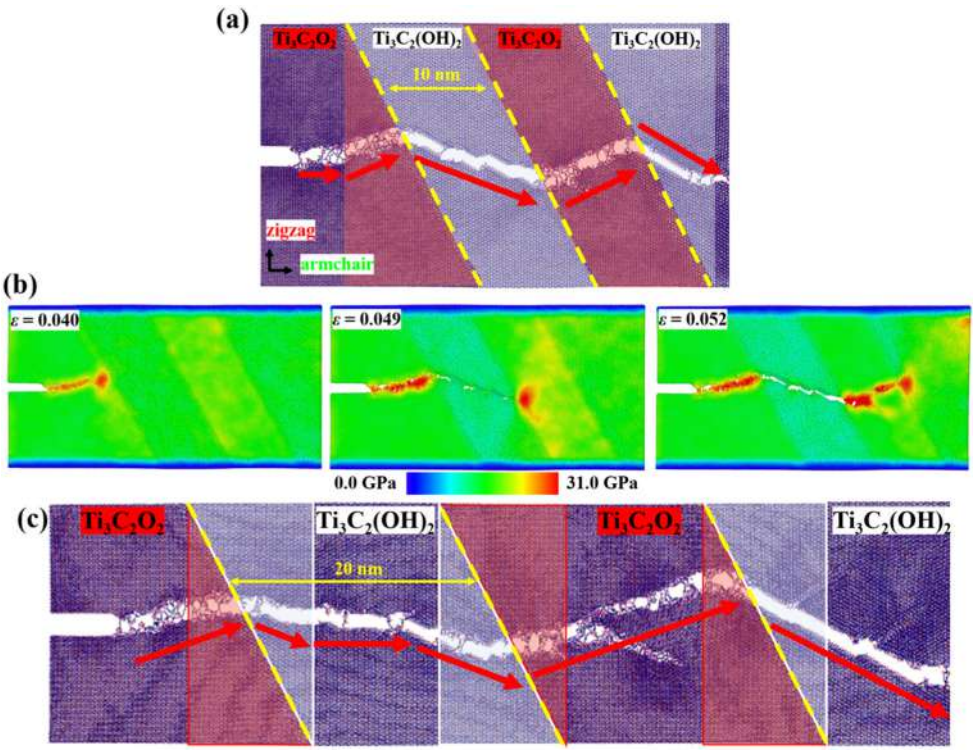

Fig. 5 The crack propagation through multiple functional group interfaces. (a) Snapshots of the crack propagation path. The red arrows represent the crack propagation directions. The distance between the interfaces was 10 nm. (b) The distribution of the average absolute stress value in the *y*-direction (σ_{yy}) when the crack propagated through the three interfaces. (c) Snapshots of the crack propagation path and the distance between the interfaces was 20 nm. The red arrows represent the crack propagation directions of the simulation results.

along the zigzag direction, the crack would go upwards, and be deflected whenever it went through the interface. A similar observation could be made if the initial crack was located in the area of $Ti_3C_2(OH)_2$ (Fig. S7b†). Close scrutiny revealed that in the area of $Ti_3C_2(OH)_2$, the crack propagation path switched between the armchair (horizontal) direction and the zigzag direction, and in the area of $Ti_3C_2O_2$, there was the formation of atomic networks and chains. These were consistent with the observation from Fig. 3a. A further analysis of stress in the y-direction (σ_{yy}) is shown in Fig. 5b.

During the crack propagation, the stress concentration would occur in the interface. And this stress concentration would lead to the crack expanding in the S2 zigzag direction in the $Ti_3C_2O_2$ area. While the stress concentration caused by the interface would occur in the S1 zigzag direction in the $Ti_3C_2(OH)_2$ area, and the crack propagation would switch from the S2 direction (the direction is shown in Fig. 4d) to the S1 direction when it came through the interface. Thus, we could draw the conclusion that wherever the crack initiated, as long as the sample was loaded along the zigzag direction, the crack would be deflected when it went through the interface. Based on this observation, we wondered if we could manipulate the crack path by varying the length of the stacking area. Thus we created another model as shown in Fig. 5d (the initial structure is shown in Fig. S7c†). In this model, similarly, the $Ti_3C_2(OH)_2$ and $Ti_3C_2O_2$ areas were stacked, however, the distance between the two interfaces is doubled compared with the model shown in Fig. 5a. Based on our simulation, we could find that the deflection behavior also happened with this model. Thus we drew the conclusion that stacking $Ti_3C_2(OH)_2$ and $Ti_3C_2O_2$ areas could be a possible approach to control the crack path of $Ti_3C_2T_2$.

4. Conclusions

We calculated the Young's modulus and shear modulus of MXenes ($Ti_3C_2T_x$), and compared the MXenes terminated by different single types of surface termination (–O, –OH). We note here that due to the limitation of existing atomistic potentials, we could not carry out a study of the properties of MXenes with –F terminations. The development of a proper atomistic potential including the interaction between F and other atoms in MXenes is a problem that needs to be solved in future work. We found that the surface terminations affected the mechanical properties of MXenes, including the magnitude of the Young's modulus, shear modulus and ultimate strength. The MXenes with –O functional groups would have a higher strength. At the linear deformation state, the most stretched bond was the Ti–T (functional group) bond, which accounted for the different elastic modulus. At the nonlinear deformation state, the Ti–C bond perpendicular to the zigzag direction was elongated substantially. As a result, the MXenes tended to crack along the zigzag direction. The fracture properties of MXenes with –O and –OH functional groups were also different and the crack propagation path also closely depended on the loading direction. The interface of the functional groups would deflect the propagation path to another zigzag direction when loaded along the zigzag direction. And the crack propagation of the MXene could be controlled by varying the functional group distribution; we hope these findings will benefit the further control of MXene fracture properties on the atomic scale and the design of nanodevices and nanocomposites using MXenes.

Author contributions

X. Y. conceived and designed the project; Y. C. carried out the simulations; Y. C., S. T., and X. Y. analyzed the data and wrote the manuscript. All authors discussed the results and commented on the manuscript.

Conflicts of interest

The authors declare that they have no known competing financial interest or personal relationship that could have appeared to influence the work reported in this paper.

Acknowledgements

We gratefully acknowledge the support from the National Natural Science Foundation of China (11902014) and Fundamental Research Funds for the Central Universities. We acknowledge the Information Office of Beihang University for the supply of the High Performance Computing Platform. X. Y. acknowledges insightful discussion with Prof. Xiaoding Wei from Peking University and Prof. Fatemeh Ahmadpoor from New Jersey Institute of Technology.

References

1 M. Naguib, M. Kurtoglu, V. Presser, J. Lu, J. Niu, M. Heon, L. Hultman, Y. Gogotsi and M. W. Barsoum, *Adv. Mater.*, 2011, **23**, 4248–4253.
2 X. Gao, X. Du, T. S. Mathis, M. Zhang, X. Wang, J. Shui, Y. Gogotsi and M. Xu, *Nat. Commun.*, 2020, **11**, 1–9.
3 M. Shi, P. Xiao, J. Lang, C. Yan and X. Yan, *Adv. Sci.*, 2020, **7**, 1901975.
4 X. Wang, S. Kajiyama, H. Iinuma, E. Hosono, S. Oro, I. Moriguchi, M. Okubo and A. Yamada, *Nat. Commun.*, 2015, **6**, 1–6.
5 V. Augustyn, J. Come, M. A. Lowe, J. W. Kim, P.-L. Taberna, S. H. Tolbert, H. D. Abruña, P. Simon and B. Dunn, *Nat. Mater.*, 2013, **12**, 518–522.
6 B. Rakhi, R. B. Ahmed, M. N. Hedhili, D. H. Anjum and H. N. Alshareef, *Chem. Mater.*, 2015, **27**, 5314–5323.
7 D. Sun, M. Wang, Z. Li, G. Fan, L.-Z. Fan and A. Zhou, *Electrochem. Commun.*, 2014, **47**, 80–83.

8 Y. Xie, Y. Dall'Agnese, M. Naguib, Y. Gogotsi, M. W. Barsoum, H. L. Zhuang and P. R. Kent, *ACS Nano*, 2014, **8**, 9606–9615.
9 X.-F. Yu, Y.-C. Li, J.-B. Cheng, Z.-B. Liu, Q.-Z. Li, W.-Z. Li, X. Yang and B. Xiao, *ACS Appl. Mater. Interfaces*, 2015, **7**, 13707–13713.
10 G. Cai, J.-H. Ciou, Y. Liu, Y. Jiang and P. S. Lee, *Sci. Adv.*, 2019, **5**, eaaw7956.
11 D. Wu, R. Zhao, Y. Chen, Y. Wang, J. Li and Y. Fan, *Phys. Chem. Chem. Phys.*, 2021, **23**, 3341–3350.
12 F. Shahzad, M. Alhabeb, C. B. Hatter, B. Anasori, S. M. Hong, C. M. Koo and Y. Gogotsi, *Science*, 2016, **353**, 1137–1140.
13 J. Lipton, J. A. Röhr, V. Dang, A. Goad, K. Maleski, F. Lavini, M. Han, E. H. Tsai, G.-M. Weng, J. Kong, *et al.*, *Matter*, 2020, **3**, 546–557.
14 F. Wu, H. Zheng, W. Wang, Q. Wu, Q. Zhang, J. Guo, B. Pu, X. Shi, J. Li, X. Chen, *et al.*, *Sci. China Mater.*, 2021, **64**, 748–758.
15 V. N. Borysiuk, V. N. Mochalin and Y. Gogotsi, *Nanotechnology*, 2015, **26**, 265705.
16 M. Naguib, V. N. Mochalin, M. W. Barsoum and Y. Gogotsi, *Adv. Mater.*, 2014, **26**, 992–1005.
17 N. C. Osti, M. Naguib, A. Ostadhossein, Y. Xie, P. R. Kent, B. Dyatkin, G. Rother, W. T. Heller, A. C. Van Duin, Y. Gogotsi, *et al.*, *ACS Appl. Mater. Interfaces*, 2016, **8**, 8859–8863.
18 N. C. Osti, M. Naguib, K. Ganeshan, Y. K. Shin, A. Ostadhossein, A. C. Van Duin, Y. Cheng, L. L. Daemen, Y. Gogotsi, E. Mamontov, *et al.*, *Phys. Rev. Mater.*, 2017, **1**, 065406.
19 M. Khazaei, M. Arai, T. Sasaki, C.-Y. Chung, N. S. Venkataramanan, M. Estili, Y. Sakka and Y. Kawazoe, *Adv. Funct. Mater.*, 2013, **23**, 2185–2192.
20 A. Lipatov, H. Lu, M. Alhabeb, B. Anasori, A. Gruverman, Y. Gogotsi and A. Sinitskii, *Sci. Adv.*, 2018, **4**, eaat0491.
21 H. Zhan, G. Zhang, J. M. Bell, V. B. Tan and Y. Gu, *Nat. Commun.*, 2020, **11**, 1–11.
22 D. Chen, S. Xu and Y. Kulkarni, *Phys. Rev. Mater.*, 2020, **4**, 033602.
23 Y. Zeng, Q. Zhang, Y. Wang, J. Jiang, H. Xing and X. Li, *Phys. Rev. Lett.*, 2021, **127**, 066101.
24 V. N. Borysiuk, V. N. Mochalin and Y. Gogotsi, *Comput. Mater. Sci.*, 2018, **143**, 418–424.
25 P. Chakraborty, T. Das, D. Nafday, L. Boeri and T. Saha-Dasgupta, *Phys. Rev. B*, 2017, **95**, 184106.
26 H. Yu, K. Xu, Z. Zhang, X. Cao, J. Weng and J. Wu, *J. Mater. Chem. C*, 2021, **9**, 2416–2425.
27 Q. Zhang, Y. Chen, Y. Zhang, J. Sun, M. Hu, X. Yan, K. Yuan, X. Yang and J. Li, *J. Phys. Chem. Lett.*, 2020, **11**, 9521–9527.
28 Y. Xie and P. Kent, *Phys. Rev. B: Condens. Matter Mater. Phys.*, 2013, **87**, 235441.
29 C. Shi, M. Beidaghi, M. Naguib, O. Mashtalir, Y. Gogotsi and S. J. Billinge, *Phys. Rev. Lett.*, 2014, **112**, 125501.
30 Y. Bai, K. Zhou, N. Srikanth, J. H. Pang, X. He and R. Wang, *RSC Adv.*, 2016, **6**, 35731–35739.
31 N. Zhang, Y. Hong, S. Yazdanparast and M. A. Zaeem, *2D Mater.*, 2018, **5**, 045004.
32 M. Kurtoglu, M. Naguib, Y. Gogotsi and M. W. Barsoum, *MRS Commun.*, 2012, **2**, 133–137.
33 Z. Fu, Q. Zhang, D. Legut, C. Si, T. C. Germann, T. Lookman, S. Du, J. S. Francisco and R. Zhang, *Phys. Rev. B*, 2016, **94**, 104103.
34 Z. Guo, J. Zhou, C. Si and Z. Sun, *Phys. Chem. Chem. Phys.*, 2015, **17**, 15348–15354.
35 U. Yorulmaz, A. Özden, N. K. Perkgöz, F. Ay and C. Sevik, *Nanotechnology*, 2016, **27**, 335702.
36 S. Plimpton, *J. Comput. Phys.*, 1995, **117**, 1–19.
37 A. Stukowski, *Modell. Simul. Mater. Sci. Eng.*, 2010, **18**, 015012.
38 X. Yan and P. Sharma, *Nano Lett.*, 2016, **16**, 3487–3492.
39 X. Yan, P. Cao, W. Tao, P. Sharma and H. S. Park, *J. Phys. D: Appl. Phys.*, 2016, **49**, 493002.
40 F. Darbaniyan, X. Yan and P. Sharma, *J. Appl. Mech.*, 2020, **87**, 031011.
41 C. Wei and C. Wu, *Eng. Fract. Mech.*, 2020, **230**, 106978.